



# Stabilizing the Cathode Interphase of LNMO using an Ionic-liquid based Electrolyte

Elise R. Østli<sup>+[a]</sup>, Alma Mathew<sup>+[b]</sup>, Julian R. Tolchard,<sup>[c]</sup> Daniel Brandell,<sup>+[b]</sup> Ann Mari Svensson,<sup>+[a]</sup> Sverre M. Selbach,<sup>[a]</sup> and Nils P. Wagner<sup>\*[a, c]</sup>

The ionic liquid (IL)-based electrolyte comprising 1.2 M lithium bis(fluorosulfonyl)imide (LiFSI) in N-propyl-N-methylpyrrolidinium bis(fluorosulfonyl)imide (PYR<sub>13</sub>FSI) (ILE) has been evaluated as a suitable system for the high-voltage cathode material LiNi<sub>0.5-x</sub>Mn<sub>1.5+x</sub>O<sub>4</sub> (LNMO) when cycled vs. graphite anodes. The oxidative stability of the ILE was evaluated by linear sweep voltammetry (LSV) and synthetic charge-discharge profile voltammetry (SCPV) and was found to exceed that of state-of-the-art 1 M LiPF<sub>6</sub> in 1:1 ethylene carbonate (EC):diethylcarbonate (DEC) (LP40). Improved cycling performance

both at 20 °C and 45 °C was found for LNMO | graphite full cells with the IL electrolyte. X-ray photoelectron spectroscopy (XPS) analysis showed that robust and predominantly inorganic surface layers were formed on the LNMO cathode using the ILE, which stabilized the electrode. Although the high viscosity of the ILE limits the rate performance at 20 °C, this ILE is a promising alternative electrolyte for use in lithium-ion batteries (LIBs) with high-voltage cathodes such as LNMO, especially for use at elevated temperatures.

## Introduction

LiNi<sub>0.5-x</sub>Mn<sub>1.5+x</sub>O<sub>4</sub> (LNMO) is considered a highly promising cathode material for use in high-energy and high-rate lithium-ion batteries (LIBs).<sup>[1]</sup> One of the main attributes of this electrode material is the high operating voltage of 4.7 V vs. Li/Li<sup>+</sup>.<sup>[2]</sup> Additionally, due to the moderate Ni content and absence of Co, the raw materials price of LNMO precursors is low compared to other high-energy cathode materials such as LiNi<sub>x</sub>Mn<sub>y</sub>Co<sub>z</sub>O<sub>2</sub> (NMC).<sup>[3]</sup> However, LNMO-based LIBs suffer from limited cycle life with common electrolytes, caused by both oxidative electrolyte degradation and cathode transition metal dissolution with subsequent transport to, and deposition on, the anode.<sup>[4–7]</sup>

The electrolyte commonly used in LIBs today consists of LiPF<sub>6</sub> salt in a blend of cyclic and linear organic carbonate solvents, e.g., ethylene carbonate (EC), diethyl carbonate (DEC), and dimethyl carbonate (DMC).<sup>[8]</sup> The electrochemical stability window of an electrolyte is ultimately determined by the Gibbs free energy of the involved reactants and products of any chemical or electrochemical side-reaction in the cell and is hence often narrower than the electronic structure of the reactants predicts.<sup>[9]</sup> If the operating voltage of an electrode is outside of this energy region, the electrolyte is not thermodynamically stable, and depending on the kinetics the electrolyte may decompose on the electrode surface. However, if a chemically stable and passivating solid electrolyte interphase (SEI) or cathode electrolyte interphase (CEI) is formed on the electrode surface during the first charge-discharge cycle, good battery cycling can be obtained even with electrode potentials outside of the thermodynamic stability window. Unfortunately, the CEI that is formed on LNMO through oxidation and polymerization of EC is not stable at the high operating voltage of LNMO.<sup>[10]</sup> This leads to continuous electrolyte degradation during battery operation. Additionally, LiPF<sub>6</sub> hydrolyses readily in the presence of trace amounts of water, forming corrosive HF.<sup>[11]</sup> An HF attack on the active material can in turn lead to transition metal (TM) ion dissolution which, in addition to degrading the positive active material, will interfere with the SEI properties through electrode cross-talk.<sup>[5]</sup> In addition to the low stability of the LiPF<sub>6</sub> salt, further disadvantages of carbonate-based electrolytes are the safety concerns arising from low flash point and high flammability.<sup>[12]</sup> The linear carbonates, a necessary component to reduce the melting point and viscosity, also make the electrolyte more flammable and thus a greater safety hazard.<sup>[13]</sup> Replacing the LiPF<sub>6</sub> salt with non-hydrolyzing imide anion-based salts, such as lithium bis(trifluoromethanesulfonyl)imide (LiTFSI) and lithium

[a] E. R. Østli,<sup>+</sup> Prof. A. M. Svensson, Prof. S. M. Selbach, Assoc. Prof. N. P. Wagner

Department of Materials Science and Engineering  
NTNU Norwegian University of Science and Technology  
7491 Trondheim (Norway)

E-mail: nils.p.wagner@ntnu.no

[b] A. Mathew,<sup>+</sup> Prof. D. Brandell  
Department of Chemistry – Ångström Laboratory  
Uppsala University  
Box 538, 75121 Uppsala (Sweden)

[c] Dr. J. R. Tolchard, Assoc. Prof. N. P. Wagner  
SINTEF Industry  
7491 Trondheim (Norway)  
E-mail: nils.peter.wagner@sintef.no

<sup>†</sup> These authors contributed equally to this work.

 Supporting information for this article is available on the WWW under <https://doi.org/10.1002/batt.202300085>

 An invited contribution to a Special Collection dedicated to NordBatt 2022 conference

 © 2023 The Authors. *Batteries & Supercaps* published by Wiley-VCH GmbH. This is an open access article under the terms of the Creative Commons Attribution License, which permits use, distribution and reproduction in any medium, provided the original work is properly cited.

bis(fluorosulfonyl)imide (LiFSI) has been investigated due to their better electrochemical and thermal stability. However, these imide salts are unable to sufficiently passivate the Al substrate (i.e., cathode current collector), leading to continuous Al degradation by anodic dissolution and, eventually, cell failure.<sup>[14,15]</sup> When LiPF<sub>6</sub> salt is applied, the Al current collector is passivated by the formation of a protective film (consisting of e.g., Al<sub>2</sub>O<sub>3</sub>F<sub>2</sub><sup>[16]</sup> and AlF<sub>3</sub><sup>[17]</sup>) due to reaction with HF. This passivation film allows for operation of the current collector even at high potentials.<sup>[16]</sup> Thereby, strategies to in-situ passivate the Al current collector through fluorine-containing additives, which will allow cycling in imide salt-based electrolytes, can be envisioned. Myung et al.<sup>[15]</sup> found, for example, that the addition of some HF into a TFSI/PC electrolyte changed the composition of the passivation film (from Al<sub>2</sub>O<sub>3</sub> to AlF<sub>3</sub> and AlOF) and improved the passivation state of the Al current collector.

Alternative electrolytes with a wider electrochemical stability window and/or excellent CEI formation capabilities are needed to achieve better stability towards LNMO. Electrolyte additives, such as lithium bis(oxalato) borate (LiBOB), lithium difluoro(oxalato) borate (LiDFOB), and nitriles have been shown to improve the anodic stability of carbonate-based electrolytes,<sup>[18,19]</sup> and highly concentrated stable lithium salts in carbonate solvents (e.g., LiN(SO<sub>2</sub>F)<sub>2</sub> in DMC) has been shown to improve the cycling stability of LNMO||graphite cells, also at elevated temperatures.<sup>[20]</sup> The high viscosity of concentrated electrolytes is, however, a drawback leading to extended wetting times, in particular for high-loading electrodes.<sup>[21]</sup> Several solid-state electrolytes (e.g., solid inorganic electrolytes such as Li<sub>7</sub>La<sub>3</sub>Zr<sub>2</sub>O<sub>12</sub> (LLZO)<sup>[22]</sup> or hybrid electrolytes (e.g., polyacrylonitrile-LiClO<sub>4</sub> with Li<sub>0.33</sub>La<sub>0.557</sub>TiO<sub>3</sub> nanowire<sup>[23]</sup> and cellulose-supported poly(propylene carbonate) (PPC)<sup>[24]</sup>) have been reported to be stable above 5 V vs. Li/Li<sup>+</sup>.<sup>[25]</sup> Similarly, several gel polymer electrolytes (e.g., a PPC polymer-based<sup>[26]</sup> and poly(acrylic anhydride-2-methyl-acrylic acid-2-oxirane-ethyl ester-methyl methacrylate) (PAMM)-based electrolyte<sup>[27]</sup>) display much higher oxidative stability limits than carbonate-based electrolytes. However, solid-state electrolytes suffer from issues related to poor contact with electrodes, and the implementation of solid-state electrolytes furthermore requires the addition of new steps in the battery production line (such as hot-pressing and additional coating steps).<sup>[28]</sup> The implementation of alternative liquid electrolytes with improved anodic stability is thus more feasible to enable the use of high-voltage cathodes.

Ionic liquids (ILs) are increasingly being investigated as electrolyte solvents for LiBs.<sup>[29,30]</sup> ILs consist of sterically bulky and poorly coordinated cations and anions and are hence in a liquid state below 100 °C.<sup>[30]</sup> Room temperature ionic liquids (RTILs) are, as the name implies, liquid at room temperature and do therefore not require any extra solvent. Several of the reported RTIL-based electrolytes have high oxidative stability, making them ideal for use with high-voltage cathodes such as LNMO.<sup>[29]</sup> The battery safety is furthermore improved by exchanging the very flammable carbonates with a RTIL with reduced flammability hazards and low volatility.<sup>[30,31]</sup> One

disadvantage of RTIL-based electrolytes is, however, the low room temperature ionic conductivity. Due to the high viscosity, even the highest RTIL conductivity is still lower than that of conventional carbonate-based electrolyte solutions.<sup>[29]</sup> Moreover, the Li<sup>+</sup> mobility is often comparatively restricted in ILs, leading to a low Li<sup>+</sup> transference number and concentration gradients in Li-battery cells. Additionally, even though the use of ILs allows for the use of imide salts to a larger extent than liquid carbonates, corrosion of the Al current collector still occurs above 4.5 V vs. Li/Li<sup>+</sup> in the presence of FSI.<sup>[32]</sup> The reduced solubility of Al in super-concentrated electrolytes, on the other hand, was reported to inhibit extensive anodic dissolution in acetonitrile.<sup>[33]</sup>

Promising electrochemical results with RTIL electrolytes operated at high voltages have nevertheless been reported. Electrolytes consisting of N-methyl-N-propyl pyrrolidinium (PYR<sub>13</sub>) cations with a bis(trifluoromethanesulfonyl)imide (TFSI) or bis(fluorosulfonyl)imide (FSI) anions were evaluated by Moreno et al.<sup>[34]</sup> Good ion transport properties (~10<sup>-3</sup> S/cm at -20 °C) and an electrochemical stability window of 5 V on a carbon working electrode was found. The IL-based electrolyte PYR<sub>13</sub>FSI in combination with LiFSI has shown excellent anodic stability in combination with Pt or Ni foils, up to 5.5 V.<sup>[35]</sup> However, in other works,<sup>[32]</sup> the anodic stability limit was found to be somewhat lower for a similar electrolyte, around 4.5 V, which was attributed to impurities in the LiFSI salt. Due to the smaller size of the anion, the PYR<sub>13</sub> ILs with FSI anions typically have a lower viscosity and higher conductivity than PYR<sub>13</sub> with the TFSI anion.<sup>[36]</sup> The TFSI anion on the other hand displays better thermal and electrochemical stability than the FSI anion.<sup>[37]</sup> In this context, it was shown by Appetecchi et al.<sup>[36]</sup> that the enhanced cathodic stability of PYR<sub>14</sub>TFSI (compared to that of PYR<sub>13</sub>FSI) leads to the absence of SEI formation on the graphite electrode, leading to solvent intercalation.

Electrolytes containing PYR<sub>13</sub>FSI, both as pure ionic liquids and as hybrid electrolytes in combination with e.g., carbonate solvents, have been evaluated for their compatibility with LNMO. Wu et al.<sup>[38]</sup> evaluated a hybrid electrolyte with varying IL/carbonate ratios and LiPF<sub>6</sub> concentrations. Improved LNMO||Li cycling stability (97% capacity retention after 300 cycles) and high temperature performance was reported for an electrolyte containing 3 M LiPF<sub>6</sub> in 75% carbonate solvent (1:1 EC:DEC) and 25% PYR<sub>13</sub>TFSI. Rath et al.<sup>[39]</sup> demonstrated ~85% capacity retention over 200 cycles for an LNMO||graphite cell with a PYR<sub>13</sub>-based electrolyte with an optimized Li<sup>+</sup>/TFSI/FSI ratio (2.4 M LiTFSI in PYR<sub>13</sub>FSI). Extended cycling performance (>85% capacity retention after 300 cycles) and high rate performance for LNMO||Li cells with a 1 M LiFSI in PYR<sub>13</sub>FSI electrolyte was found by Lee et al.<sup>[40]</sup> The improved capacity retention was attributed to the formation of a robust and conductive CEI on the LNMO with the PYR<sub>13</sub>FSI electrolyte. Additionally, good stability towards several anode materials (e.g., Si<sup>[41-44]</sup>, graphite,<sup>[45]</sup> and Li metal<sup>[46]</sup>) has been reported for PYR<sub>13</sub>FSI-based electrolytes. Thus, in addition to enabling the implementation of LNMO on the cathode side of the battery, the use of this electrolyte can allow for an increased Si amount on the anode side, leading to a high energy density.

In this work, a 1.2 M LiFSI in PYR<sub>13</sub>FSI electrolyte, hereby named ILE, is compared to 1 M LiPF<sub>6</sub> in 1:1 EC:DEC (v/v), hereby named LP40. The main purpose of this study is to firstly gain more information about the oxidative stability of the ILE towards C-coated Al and the LNMO electrode through electrochemical characterization by linear sweep voltammetry (LSV) and synthetic charge-discharge profile voltammetry (SCPV).<sup>[47]</sup> Secondly, since good compatibility between the ILE and graphite<sup>[45]</sup> has been demonstrated, the cycling stability in LNMO|ILE|graphite full cells is evaluated and compared to that of LNMO|LP40|graphite cells, both at 20 °C and 45 °C. The temperatures were chosen to evaluate the conductivity limitations of the ILE (20 °C) and the thermal stability at elevated temperatures (45 °C) where the LNMO|LP40|graphite system is particularly unstable.<sup>[48]</sup>

## Results and Discussion

### High voltage stability

LSV with carbon-coated Al-foil as a working electrode, and Li as a counter electrode, was conducted at 20 °C and 45 °C to compare the oxidative stability limit of the two electrolytes, as presented in Figure 1a). The voltage values reported in this section are all vs Li/Li<sup>+</sup> unless otherwise specified. At 20 °C, the LP40 electrolyte (black) displays an increase in current density at 3.7 V which stabilizes at 3.9 V before a new increase in current density is observed at 4.18 V. Before it stabilizes, an additional current density increase occurs at 4.3 V. The onset potential of the excessive increase of the oxidation current is 4.86 V. At 45 °C, the initial current increase occurs as low as 3.3 V. Before it stabilizes, the current density increases also at 4.1 and 4.2 V. The exponential increase in current density starts from 4.8 V. In contrast, the current density of the ILE (teal) at 20 °C is below 1 μA/cm<sup>2</sup> up to 4.6 V and does not exceed 2.6 μA/cm<sup>2</sup> until 5 V is reached. A small and gradual increase in current density is observed, beginning at 3.3 V and ending in a small peak at 4.3 V that stabilizes at 4.4 V. The exponential

increase in current density starts from 5 V. At 45 °C, a small gradual increase in current density is observed from 3 V, but stays below 1 μA/cm<sup>2</sup> up to 4.25 V. At potentials above 4.5 V, the current density increases more rapidly. It is clear from the LSV results that the ILE has a higher anodic stability than LP40, both at 20 °C and 45 °C, although both the ILE and LP40 have reduced anodic stability at 45 °C than at 20 °C.

Overcharge experiments of LNMO||Li cells were carried out with an upper voltage limit of 6 V. The charging curves are presented in Figure 1b). Both cells display close to identical behavior until the voltage reaches 5.3 V, where the ILE suddenly experiences a voltage drop to 4.75 V after which the voltage displayed a noisy curve between 4.98 and 4.66 V. The sudden voltage drop observed at 5.3 V was reproduced in several measurements. This behavior is different from LP40, which displays an increase in voltage until a plateau is reached at 5.4 V. This is slightly lower than the stability limit measured by Kasnatscheew et al.<sup>[49]</sup> where LNMO|LP50|Li (LP50: 1 M LiPF<sub>6</sub> in 1:1 EC:ethyl methyl carbonate (EMC)) displayed a voltage plateau at ~5.6 V. Based on the overcharge experiment, the ILE behaves stably up to 5.3 V, before a voltage drop to 4.75 V and concurring oxidation was reproducibly observed. We suggest this behavior is caused by a kinetic barrier after which corrosion of the current collector occurs at 4.75 V vs. Li/Li<sup>+</sup>.

The SCPV approach was utilized to evaluate the oxidative stability of the electrolytes used in this work, as well as their ability to form a passivation layer on the LNMO electrode. This method employs the voltage profile of the active material of interest, in this case, LNMO, and applies it to a system with an inert electrode, here carbon-coated aluminum, to accurately mimic the voltage variations over time as those experienced in a real LNMO half-cell. The LNMO voltage profile was divided into two regions: the upper plateau region (>4.3 V) and the lower plateau region (<4.3 V) as shown in Figure 2a), for both anodic and cathodic SCPV sweeps. It should be noted that compared to the lower plateau region, the time spent at the higher plateau region, which corresponds to the Ni<sup>2+</sup>/Ni<sup>3+</sup> and Ni<sup>3+</sup>/Ni<sup>4+</sup> redox couples in LNMO cells, is longer, and thereby better mimics the true cell behavior than if the potential is

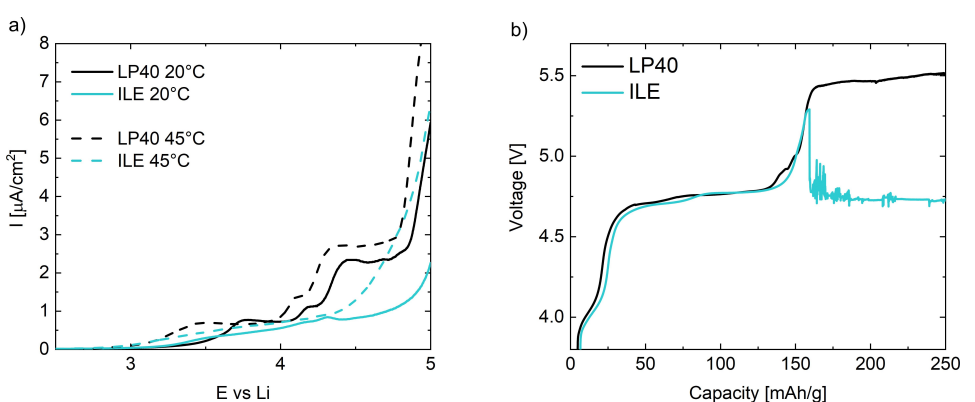


**Figure 1.** a) LSV curves of Li|LP40|carbon-coated Al foil (black) and carbon-coated Al foil|ILE|Li (teal) at 20 °C (solid) and 45 °C (dashed). b) Overcharging experiment of a LNMO half-cell containing LP40 (black) and ILE (teal) with a C-rate of C/10 at 20 °C. The upper voltage limit of 6 V vs. Li/Li<sup>+</sup> is not reached due to continuous electrolyte oxidation and/or current collector corrosion respectively.

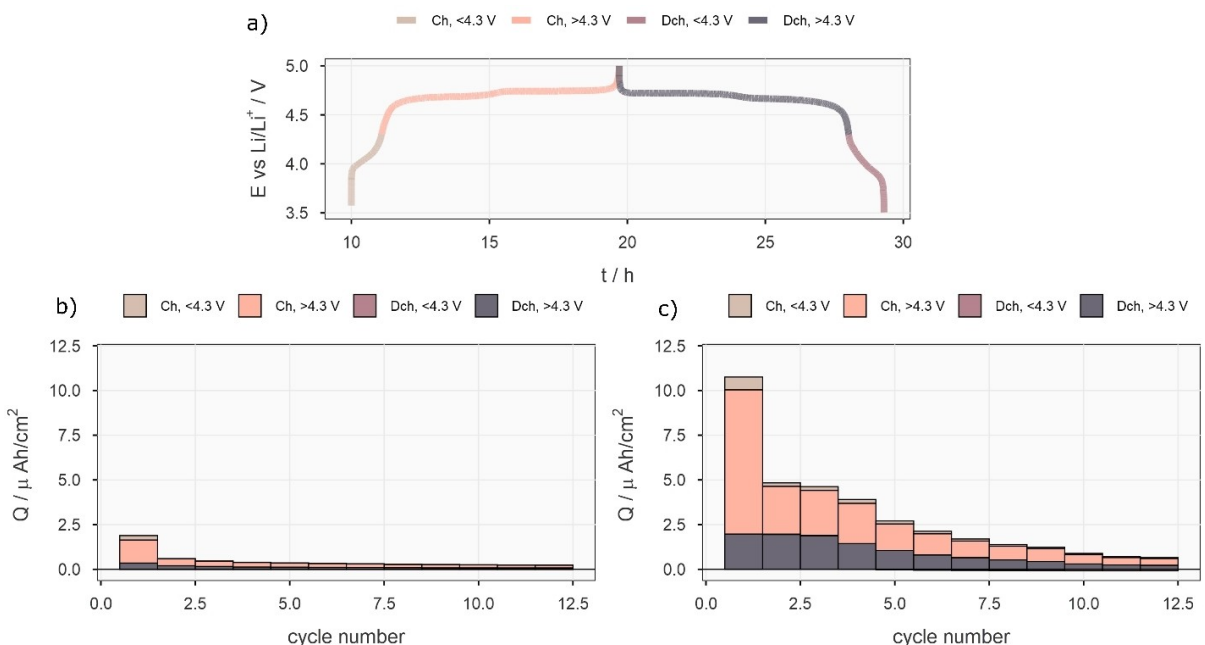


**Figure 2.** a) Voltage profile of the LNMO half-cell and multiple SCPV cycles with cells containing b) ILE (see Figure S1 for zoomed in data) and c) LP40 as electrolyte. The cells contain carbon-coated aluminum as the working electrode and Li as both counter and reference electrode.

swept uniformly. Figure 2(b and c) shows the amount of charge that is passed in each region for the ILE and the LP40-based cells, respectively. In both the anodic and cathodic sweeps, it is observed that the LP40-based cell passed a higher quantity of charge in both regions. The total quantity of charge passed in the first cycle for the LP40-based cell is more than  $10 \mu\text{Ah cm}^{-2}$ , whereas the ILE-based cell corresponds to less than  $2.5 \mu\text{Ah cm}^{-2}$ . The quantity of charge passed can be correlated to the magnitude of electrolyte degradation taking place in the cell. The increased charge in the upper plateau region suggests that the LP40 electrolyte has oxidized to a larger extent than the ILE. The quantity of charge passed in subsequent cycles likewise reveals that the LP40-based cell also passes a higher amount of charge than the ILE-based cell. It is worth noting that the total amount of charge passed in the LP40-based cell becomes constant after about 10 cycles, whereas it becomes constant in the ILE-based cell already after the third cycle. The evolution of charges being nearly constant indicates the formation of a stable passivation layer.

#### Galvanostatic cycling of LNMO || graphite cells

The ionic conductivity of the ILE is reported to be  $5 \text{ mS cm}^{-1}$  at  $20^\circ\text{C}$ , which is less than half of regular LiB electrolytes, with only a fraction of the cation current being attributable to Li ions.<sup>[50]</sup> To elucidate the effect of limited conductivity on the rate acceptance, LNMO || graphite full cells were rate-tested at both  $20^\circ\text{C}$  and  $45^\circ\text{C}$ . Initially, the cells were cycled at C/10, before the C-rate was increased to C/5, C/2, 1 C and 2 C before being reduced to C/10 again. The C-rate on charge was identical to the discharge rate up to C/2. For higher discharge

rates the C-rate on charge was kept at C/2 to prevent Li plating. The discharge voltage profiles are shown in Figure 3(a-d) (the capacity as function of cycle number and the corresponding C/10 voltage profile are shown in Figures S2 and S3). Although the high viscosity of ILE compared to LP40 can lead to limited rate performance, this is not visible at  $20^\circ\text{C}$  until the discharge rate reaches 2 C. Here, the discharge capacity of ILE is reduced to  $45 \text{ mAh/g}$  while LP40 delivers  $83 \text{ mAh g}^{-1}$ . It must be pointed out that the full cells were balanced to  $\sim 1 \text{ mAh cm}^{-2}$ , and a reduced rate performance using ILE at  $20^\circ\text{C}$  can be expected with higher electrode loadings due to the high viscosity of ILE. Accelerated capacity fade can be observed after 20 cycles in the case of LP40, even when the C-rate is reduced to C/10. The ILE-based cell, on the other hand, retains a capacity of  $114 \text{ mAh g}^{-1}$  at the end of the rate program with a C-rate of C/10. The Coulombic efficiencies at  $20^\circ\text{C}$  are generally higher for ILE, apart from the first cycle Coulombic efficiency, where LP40 (83.6%) is slightly above ILE (83.2%). The SCPV results are in good agreement with the Coulombic efficiency values and can partly explain why the LP40-based cells have a lower Coulombic efficiency and indicate stable CEI formation with the ILE. Each increase in C-rate is accompanied by a small, reversible drop in Coulombic efficiency and capacity for both LP40 and ILE, but this effect is more pronounced for ILE, in particular when the C-rate is increased to 2 C.

The differences in performance of LNMO || Graphite cells with LP40 and ILE electrolytes are more visible at  $45^\circ\text{C}$ , as seen in Figure 3(b and d). The ILE-based cell cycled with capacities between 113 and  $95 \text{ mAh/g}$  at all rates. In contrast to the LP40 cell, which showed a steep decline in capacity during the first 5 cycles (from 102 to  $72 \text{ mAh g}^{-1}$ , Figure S2) and delivered a capacity of only  $32\text{--}44 \text{ mAh g}^{-1}$  at the higher C-rates. The

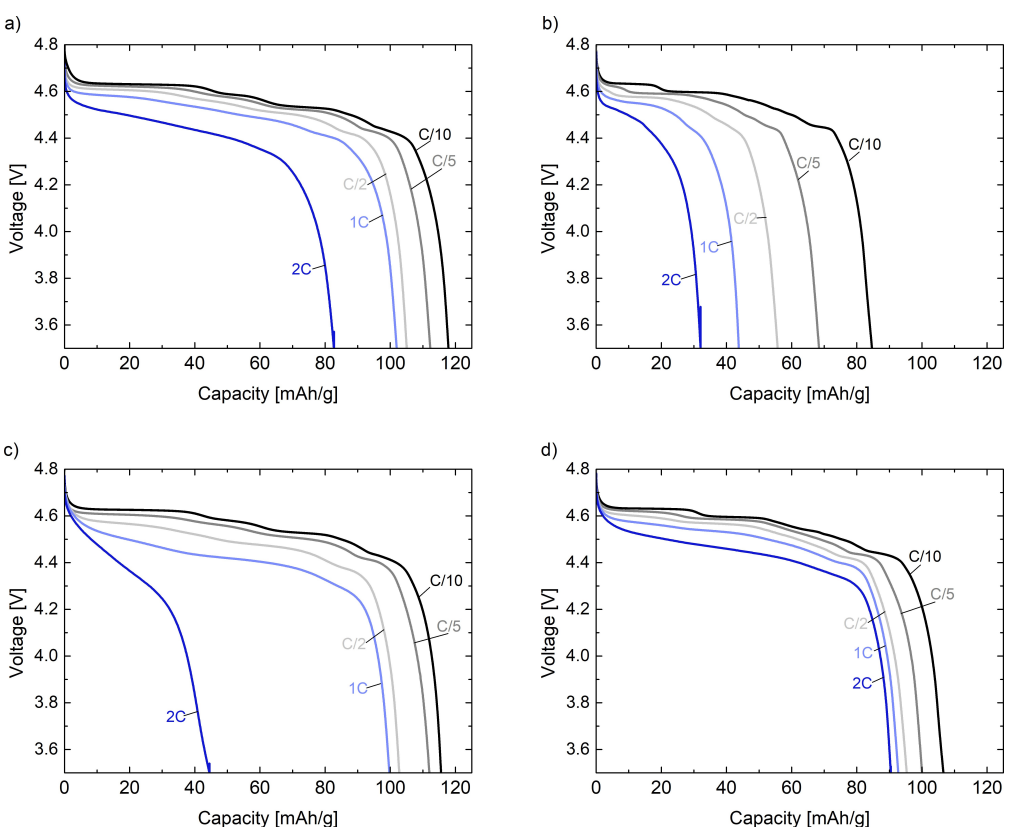


**Figure 3.** Discharge curves of LNMO || graphite cells with LP40 electrolyte cycled at a) 20 °C and b) 45 °C, and ILE electrolyte cycled at c) 20 °C and d) 45 °C. The C-rates are indicated in the figures.

capacity decline can be attributed to extensive electrolyte degradation observed for LP40 in the LSV results at 45 °C.

The cycling stability and coulombic efficiency of the LNMO|LP40|graphite and LNMO|ILE|graphite at 20 °C and 45 °C for 250 cycles, are illustrated in Figure 4. The voltage profiles of cycle 3 (C/10) and all second diagnostic cycles at C/10 (see experimental section) are shown in Figure S4 in the supporting information. The first cycle loss for the LP40 cell at 20 °C during formation at C/10 was ~27 mAh g<sup>-1</sup> with a reversible capacity of 119 mAh g<sup>-1</sup> (LNMO). After three initial C/10 cycles, the rate was increased to C/2 with an initial discharge capacity of 113 mAh g<sup>-1</sup> (LNMO). The cell showed a steady decline in reversible capacity and after 85 cycles the capacity decayed to 80% of its initial C/2 value, indicating rapid loss of the Li inventory. This is evident in the C/10 voltage profiles (Figure S4a), where the first voltage plateau on discharge attributable to Ni<sup>+3/+4</sup> in LNMO and stage 1 LiC<sub>6</sub>-LiC<sub>12</sub> becomes shorter with increasing cycle number. For the ILE cell, the first cycle loss upon formation at 20 °C was ~26 mAh g<sup>-1</sup> with a reversible capacity of 116 mAh g<sup>-1</sup> (LNMO). At C/2, the cell delivered an initial capacity of 113 mAh g<sup>-1</sup> (LNMO), with 86% capacity retention after 250 cycles at C/2, showing superior performance with respect to room temperature stability of the ILE electrolyte in the LNMO || Graphite system.

The first cycle loss in graphite-based cells is predominately related to the SEI formation by electrolyte reduction<sup>[51]</sup> consuming active Li.<sup>[52]</sup> There is no large difference in the first

cycle losses between the two electrolytes at 20 °C. However, upon first charge the cell using the FSI-based ILE showed a feature at lower potentials compared to the LP40-based cells (Figure S5), in line with the higher reduction potential of FSI.<sup>[53]</sup> Furthermore, earlier studies on FSI-based electrolytes have shown a SEI with higher fraction of inorganic species.<sup>[54]</sup> The more stable cycling of the ILE-based cell suggests generally lower levels of parasitic side reactions causing gassing, inventory loss and increased cell impedance. This is reflected in the Coulombic efficiency data (Figure 4c) where the Coulombic efficiency of the ILE cell reaches values above 99.9% after a few cycles while the LP40-based cell takes more cycles before the coulombic efficiency stabilizes around 99.6%–99.7%. Under accelerated degradation conditions at 45 °C (Figure 4b; for clarity 250 cycles shown. All cycles are shown in Figure S6), the LP40-based cell showed a low reversible capacity of 97 mAh/g and a severe first cycle loss of 45 mAh/g suggesting a high level of irreversible side reactions on the first charge. In the second cycle at C/10 the capacity further decayed to 85 mAh g<sup>-1</sup>, with a low Coulombic efficiency of 90% suggesting that the combination of slow charge, and hence long times spent at highly oxidizing potentials, and elevated temperatures is detrimental to the cell. This is also visible in the voltage profile, where the polarization at the end of charge shows a more sloping behavior compared to the other tests, indicating side reactions at high potentials (Figure S4c). Not surprisingly, a further drop to 74 mAh g<sup>-1</sup> is observed when switching to C/2,

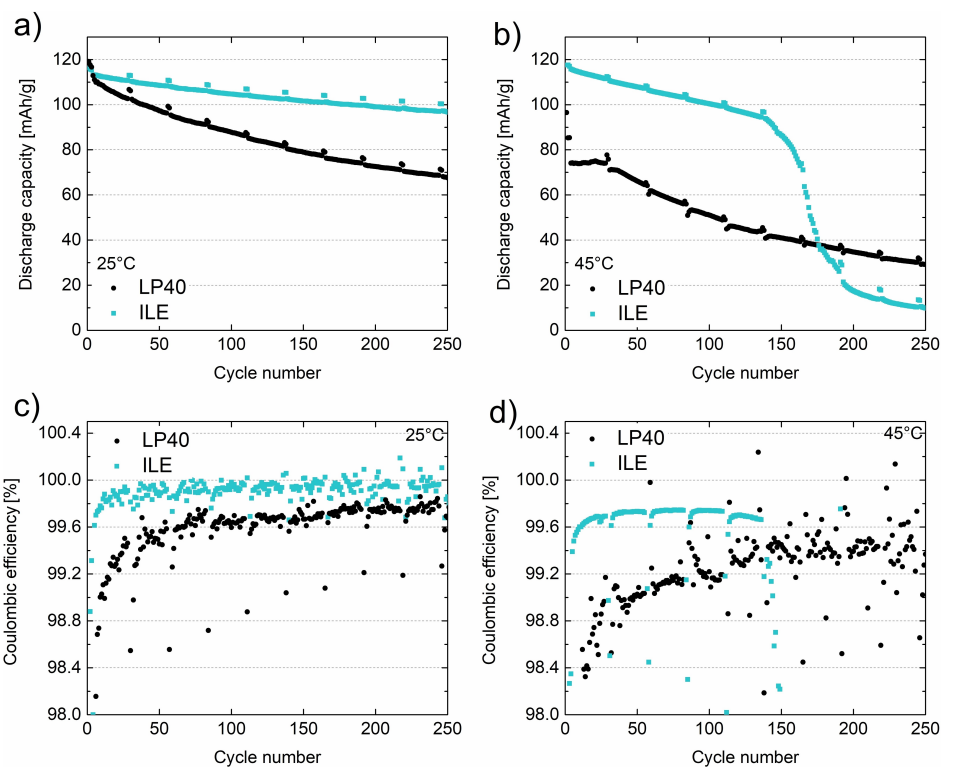


**Figure 4.** Discharge capacities of LNMO | | graphite cells tested at a) 25 °C and b) 45 °C. The corresponding Coulombic efficiencies are shown in c) and d), respectively.

likely caused by increased cell impedance due to electrolyte degradation. The cell cycled stably at this value for 25 cycles and only minor recovery was detected when switching back to C/10. After increasing the rate again to C/2, the cell showed a steady decay in reversible capacity, and after 250 cycles only 29 mAh/g<sup>-1</sup> could be recovered. This is reflected in the low Coulombic efficiency (Figure 4d) between 98.9% and 99.4%. The cell cycled with ILE electrolyte showed a first cycle reversible capacity of 118 mAh/g<sup>-1</sup> with an irreversible loss of 27 mAh g<sup>-1</sup>. These values are close to identical with room temperature cycling. After formation the capacity was 116 mAh g<sup>-1</sup> at C/2. However, a slow and linear decline in the reversible capacity was observed and after 139 cycles a reversible capacity of 94 mAh g<sup>-1</sup>, corresponding to 81% retention, was recovered. At this point a drastic drop in reversible capacity was observed. This phenomenon is often called ‘rollover failure’, which can be caused by anode pore clogging and Li inventory loss due to transition metal crosstalk triggered electrolyte decomposition.<sup>[55,56]</sup> The Coulombic efficiency (Figure 4d) of 99.7% was also lower than for the cell cycled at room temperature. Interestingly, the capacity decay was lower than the CE value would suggest. This might be connected to the nature of the ILE electrolyte consisting entirely of cations and anions, since side reactions that would usually cause Li inventory loss might instead consume the PYR<sub>13</sub> cation of the ILE electrolyte. In addition, a lower Coulombic efficiency of ~99% was detected during the slow cycles at C/10 suggesting more degradation by the increased

time at high potentials, in contrast to cycling at room temperature.

#### CEI composition and high temperature postmortem analyses

The formation and composition of the cathode electrolyte interphase (CEI) on the LNMO electrodes cycled with both LP40 and ILE was studied using X-ray photoelectron spectroscopy (XPS). The data from a pristine LNMO electrode with no contact with electrolyte and LNMO electrodes cycled with either LP40 or ILE for up to 40 cycles are shown in Figure 5.

The strongest peak in the C1s spectrum of the pristine electrode is assigned to carbon black and is located at 284.8 eV. All spectra were calibrated with respect to this peak. PVdF-HFP was used as a binder for the LNMO electrodes, and all peaks resulting from the binder in all C1s spectra are colored light blue for clarity. Species C–O and C=O adsorbed on the electrode are marked as a brown peak at 285.2 eV and a red peak at 288.6 eV, respectively. In terms of shape and composition, the C1s spectra from the pristine electrode and the electrode cycled with LP40 are comparable, indicating that there are primarily insignificant differences between the samples regarding components making up the organic parts of the CEI layer. The C1s spectrum of the cathode cycled with ILE has a comparable composition to the pristine and electrode cycled with LP40, but the intensities are different, resulting in a different peak shape. Overall, this suggests that a more inorganic CEI is formed when using the ILE. The O1s spectrum

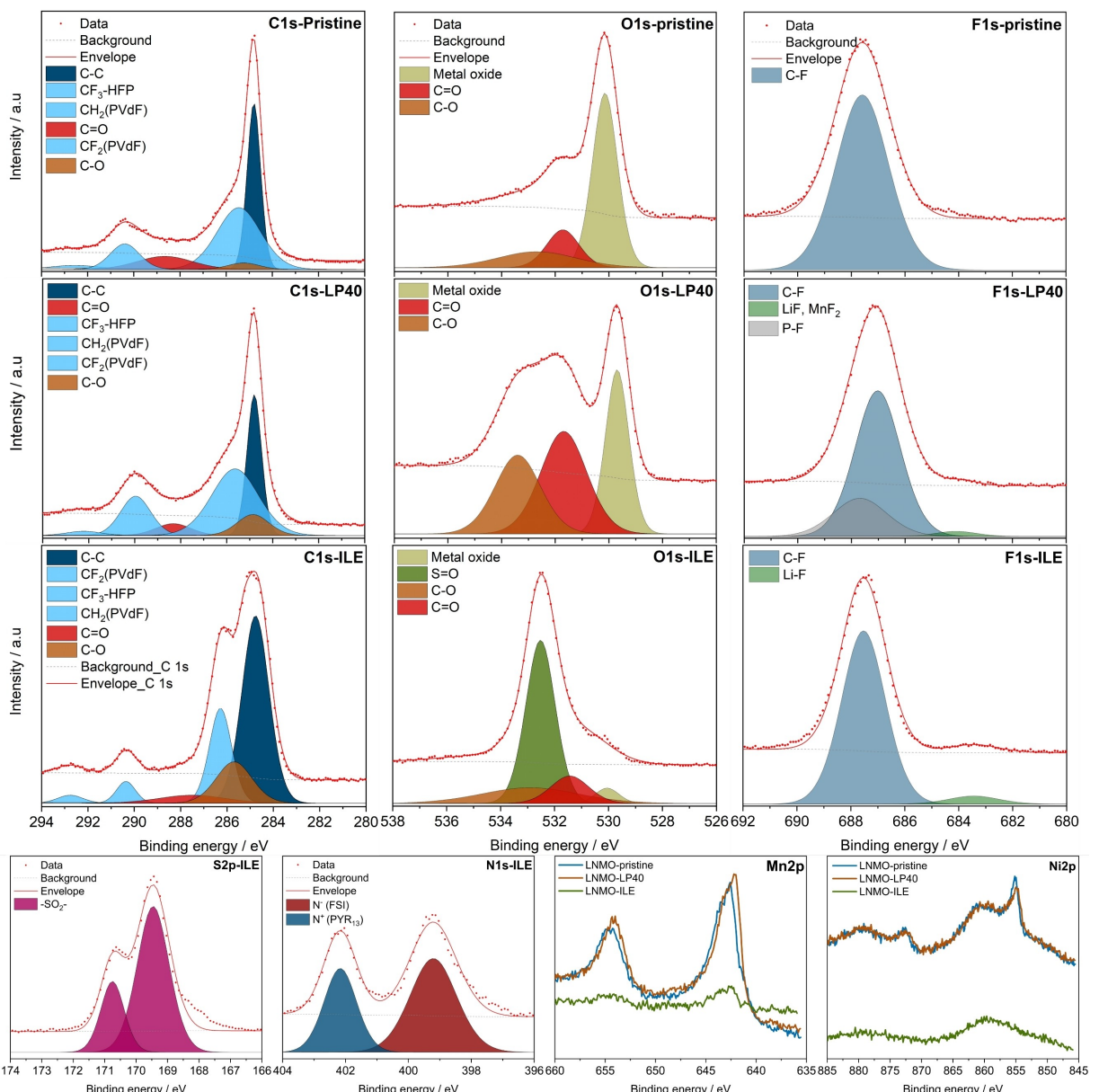


**Figure 5.** Deconvoluted XPS spectra of C1s, O1s, F1s, S2p, N1s, Mn2p and Ni2p of LNMO electrodes – pristine, and cycled with either LP40 or ILE for 40 cycles.

of the pristine LNMO electrode shows a strong peak at 530.1 eV originating from metal oxides and adsorbed C=O and C=O species at 532.6 eV and 531.7 eV, respectively.<sup>[57]</sup> C=O and C=O species show increased intensity in the O1s spectrum after 40 cycles with the LP40 electrolyte, as compared to the peak from metal oxides, indicating decomposition of the carbonate solvents. The O1s spectrum for the LNMO electrode cycled with ILE suggests a sharp and intense peak at 532.5 eV which corresponds to S=O species, that is most likely originating from decomposition of FSI anions. The relative decreased intensity of the metal oxide species is intriguing since it suggests the formation of a thicker surface layer on LNMO electrode using an ILE. The F1s XPS spectra of the pristine LNMO electrode shows just one peak at 687.5 eV arising from C–F species from the PVDF-HFP binder. In the F1s spectrum of the electrode

cycled with LP40 electrolyte, the subtle peak at lower binding energy, i.e., 683.8 eV, suggests LiF and MnF<sub>2</sub> species arising from LiPF<sub>6</sub> decomposition. This accords with attribution of the peak at 685.4 eV to lithiated fluorophosphates (Li<sub>x</sub>PO<sub>y</sub>F<sub>z</sub>), also from LiPF<sub>6</sub> salt decomposition.<sup>[40,58]</sup> In the case of the electrode cycled with ILE, the lower intensity peak at 683.4 eV indicates the presence of LiF inorganic species, which is a crucial component for the stable formation of a CEI and decreases the possibility of any further electrolyte side-reactions.<sup>[59]</sup> The CEI formation on the LNMO electrode cycled with ILE is aided by the ionic liquid electrolyte decomposition forming a largely inorganic interfacial layer, as evidenced by the N1s and S2p spectra. Two peaks can be seen in the S2p spectrum at 169.4 eV and 170.7 eV, which correspond to S2p<sup>3/2</sup> and S2p<sup>1/2</sup>, respectively. The presence of SO<sub>2</sub> in the CEI layer is supported

by these peaks, as well as S=O species found in the O1s spectrum. The SO<sub>2</sub> environment, which is most likely a breakdown product of the FSI anion from the ionic liquid, is known to improve the stability of the interphase.<sup>[40]</sup> The presence of N-containing species from FSI anions, as well as from the cationic part (PYR<sub>13</sub>) of the ionic liquid, is indicated by the two distinct peaks at 399.2 eV and 402.1 eV in the N1s spectrum.

Furthermore, Mn2p and Ni2p spectra of all three electrodes are shown in Figure 5. The relatively lower intensity of both Mn2p and Ni2p signals in the electrode cycled with ILE compared to the pristine electrode and the electrode cycled with LP40, indicates the presence of a thicker CEI. The shift observed in the Mn2p spectrum towards lower binding energy in the LNMO electrode cycled with LP40 as compared to the pristine electrode suggests a side-reaction involving Mn. Any trace water in the electrolyte that combines with the LiPF<sub>6</sub> salt in the LP40 electrolyte can generate HF, which eventually leads to the reduction of Mn<sup>4+</sup>. Interestingly, the Mn2p spectra of the electrode cycled with ILE does, on the other hand, not appear to shift as much to a lower binding energy as the LP40-based electrode. This shows that the LP40-based electrode forms a less stable CEI even after 40 cycles, while the ILE-based electrode forms a relatively stable CEI which is in line with the improved capacity retention of the LNMO || graphite cell cycled with ILE at 20 °C.

The cell cycled in ILE showed improved performance under accelerated ageing conditions at 45 °C. However, a decreased Coulombic efficiency was detected, and the cell eventually suffered from rollover type failure. To gain further insights on the degradation, post-mortem SEM-EDS analyses of cells cycled with both types of electrolytes were performed. Figure 6 compares the surfaces of LNMO cathode particles cycled at 45 °C in both LP40 and ILE, with a pristine electrode. SEM-EDS element maps for the electrodes cycled at 45 °C are shown in Figure 7 for cells cycled using LP40 and ILE electrolytes. For comparison, equivalent mapping of a pristine electrode and quantification of the summed X-ray microanalysis data collected over the mapping areas are shown in Figure S7 and Table S1, respectively, in the Supporting Information.

It is clear from the electron microscopy examination that the performance degradation observed in the electrochemical tests is accompanied by substantial electrolyte degradation. This can be easily observed visually, with a build-up of CEI visible on the LNMO particles cycled in both LP40 and ILE (Figure 6). The conductive carbon/binder phase of the cathode cycled in LP40 shows further enrichments in P, suggesting side reactions occurring preferentially (Figure 7). Though not obvious from the maps (Figure 7), a distinct increase in the fluorine concentration in this conductive carbon/binder phase is observed in local quantitative analysis, with the F:C ratio (wt:wt) increasing from approx. 0.12:1 in the uncycled and ILE electrodes to approx. 0.17:1 in the cathode cycled with LP40. The correlation of fluorine and phosphorus accords well with the expected decomposition of the LiPF<sub>6</sub> salt.

The cell cycled in ILE on the other hand shows the appearance of a Sulphur-rich gel/polymeric phase spanning between the active cathode particles while also covering them

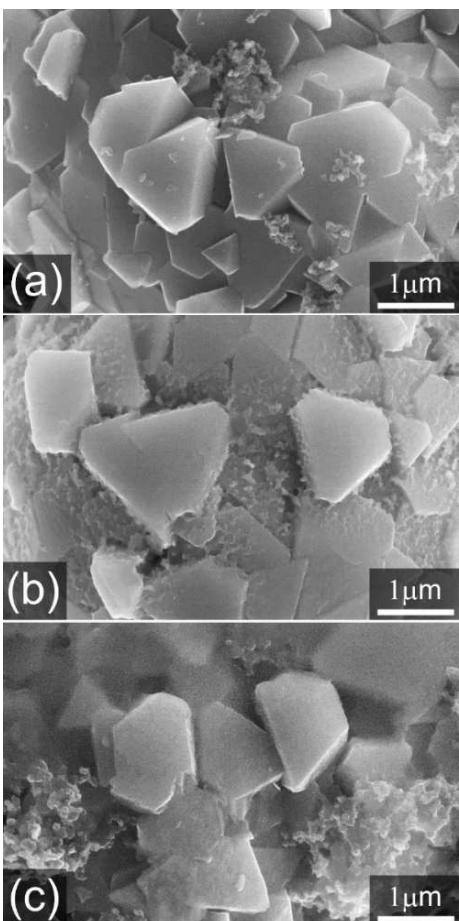


**Figure 6.** Secondary electron images of the surface of LNMO in a) a pristine electrode, b) an electrode after extended cycling at 45 °C in LP40 electrolyte and c) extended cycling at 45 °C in ILE.

(Figures 6 and 7). Ratios of S:C and N:C (wt:wt) in the range 0.2:1 to 0.3:1 were measured in the gel-like areas shown in Figure 7, which strongly suggests polymerization of the ionic liquid to form this phase.

The SEM-EDS mapping data for the corresponding anodes is presented in Figure S8 in the supporting information. It is clear from the high magnification images that both cycled anodes additionally show extensive SEI build-up. The anode degradation film on the electrode cycled in LP40 seems visibly denser than for the electrode used with ILE, which appears more porous. For the anode used with the ILE, needle-like depositions are also observed (Figure S9) which are characteristic of lithium plating/deposition.<sup>[55]</sup> As these are visible at the SEI surface, it may be speculated that these form after the rollover observed in Figure 4(b) and are a consequence of a resulting overpotential.

In agreement with previous reports,<sup>[60]</sup> deposition of manganese at the anode is detected (Table S1) for the cell using the organic carbonate electrolyte but is worse for the cell which used ILE. However, the amount of charge passed through this cell is much higher compared to the cell cycled in LP40, as it upheld a high reversible capacity for 139 cycles.

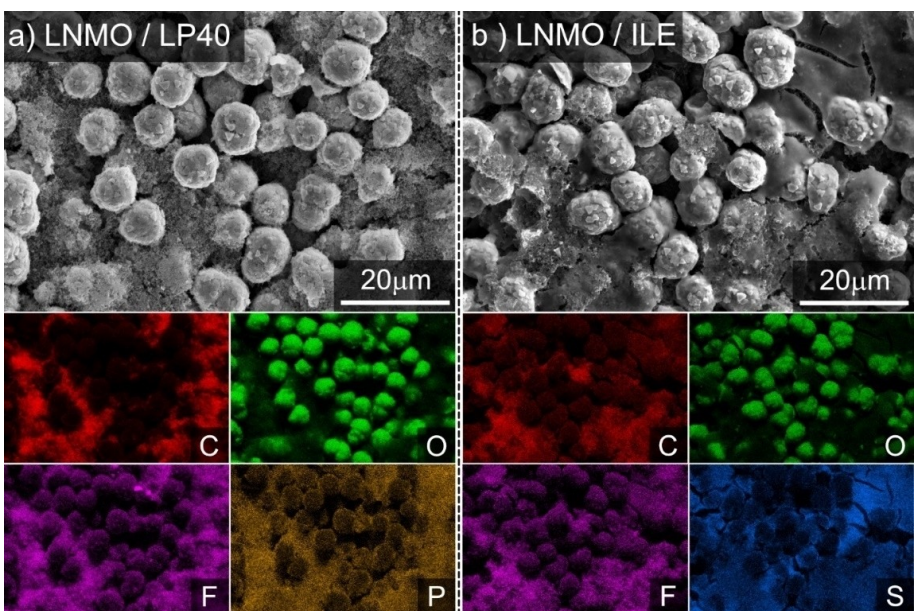


**Figure 7.** Secondary electron image and corresponding EDS maps of the surface of LNMO cathodes after prolonged cycling against a graphite anode at 45 °C in a) LP40 and b) ILE.

Also evident at the anodes is a non-negligible level of aluminium, with a higher overall Al concentration observed at the anode for the LP40 electrolyte cell. For the anode cycled in ILE, “hot spots” are evident in the map at sites where it seems that Al has been reduced. Associated to the Al hot spot regions is a higher concentration of S detected, which could suggest electrolyte decomposition. Al is known to alloy with Li below 0.5 V resulting in high volume expansion, which in turn can cause SEI damage and consequent electrolyte degradation.<sup>[6]</sup> SEM images of the carbon coated Al current collector (Figure S10) confirm pitting, characteristic of anodic dissolution and likely assisted by the pressing of the active material onto the current collector. With severe degradation present on both electrodes, it cannot ultimately be concluded which phenomenon caused the rapid decay in reversible capacity after relatively stable cycling for 139 cycles. However, these phenomena are likely connected, and the relatively low CE values suggest ongoing side-reactions also during apparently “stable” operation of the cell.

## Conclusions

The anodic stability limits of both LP40 and ILE on carbon-coated Al-foil, obtained by LSV decrease at elevated temperature (45 °C) compared to room temperature (20 °C). Analysis by LSV and SCPV indicate less parasitic currents for ILE compared to LP40 below 5 V vs. Li/Li<sup>+</sup>. Additionally, the SCPV results showed that ILE forms a stable CEI on the carbon-coated Al at relevant potentials after only a few charging cycles, while LP40 is overall less stable, and does not stabilize until after 10 cycles. The improved CEI layer formation of ILE as compared to LP40 is also corroborated by XPS analysis, which shows a

considerably more inorganic CEI layer for ILE. These observations are supported by the rate-testing of LNMO|LP40|graphite full cells, which display lower Coulombic efficiencies than LNMO|ILE|graphite, both at 20 °C and 45 °C. The rate performance of ILE and LP40 was similar at 20 °C up to discharge C-rates of 1 C, but a low discharge capacity was obtained for ILE at higher current rates. At room temperature, LNMO|LP40|graphite cells suffered from capacity fade and retained 80% of the initial capacity after only 85 cycles. In contrast, the ILE based cell had a capacity retention of 86% after 250 cycles. At accelerated ageing conditions at 45 °C, ILE based cells displayed superior rate performance and cycling stability compared to LP40 based cells. The ILE based cells had a capacity retention of 81% after 139 cycles, whilst the LP40 based cell suffered from severe capacity decay from the first cycle on. However, the ILE based cell suffered from rollover type failure and postmortem SEM-EDS analyses revealed ongoing side reactions highlighting the importance of the time the cell is exposed to high oxidizing potentials at elevated temperature.

## Experimental Section

Electrode slurries with 90 wt% LiNi<sub>0.43</sub>Mn<sub>1.57</sub>O<sub>4</sub> (LNMO) (Haldor Topsøe, Denmark), 5 wt% carbon black (Imerys C-nergy Super C 65) and 5 wt% Kynar Flex HFP2801 PVdF-HFP dissolved in N-methyl-2-pyrrolidone (NMP) were produced by slurry mixing using a Retsch MM400 shaker mill with three ZrO<sub>2</sub>-balls (5 mm) at 25 Hz for 20 minutes. The slurries were coated onto 22 μm thick carbon-coated Al foil (SDX, ShowaDenko) with a gap size 200 μm and dried overnight at 60 °C. The typical active material electrode loading was ~7 mg cm<sup>-2</sup>. Disk-shaped electrodes were cut and further densified at ~15–20 MPa for 3 min using a uniaxial press. Cell assembly was carried out in an Ar-filled glove box (O<sub>2</sub> and H<sub>2</sub>O

levels <0.1 ppm). Prior to cell assembly, the electrodes were dried at 120 °C under vacuum for 12 h. The reference standard LP40 electrolyte was 1 M LiPF<sub>6</sub> in EC/DEC = 50/50(v/v) (battery grade, Sigma Aldrich). The ionic liquid electrolyte (ILE) was prepared by dissolving 1.2 M lithium bis(fluorosulfonyl)imide (LiFSI) (>99%, American Elements) in N-propyl-N-methylpyrrolidinium bis(fluorosulfonyl)imide (PYR<sub>13</sub>FSI) (99.9%, Solvionics). The viscosity of the pure PYR<sub>13</sub>FSI is stated as 52.7 mPa·s at 25 °C by the supplier. Half- and full cells were assembled in a single layer pouch cell format containing Celgard 2325 separators for LP40 or Evopor 5E02 A (30 µm, Lydall) separators for ILE soaked in 50 µL of the respective electrolyte. Li metal foil (0.75 mm, Alfa Aesar) or graphite electrode laminates on Cu-foil (1.1 mAh cm<sup>-2</sup>, CustomCells®, Germany) acted as counter electrodes. The LNMO||graphite full cells were balanced with a negative (N) to positive (P) capacity ratio (N/P) of approximately 1.16, where 1 C corresponds to 130 mAh g<sup>-1</sup> (LNMO).

Galvanostatic overcharge of LNMO||Li half-cells was carried out with a C-rate of C/10 for 20 h and an ultimate cut-off of 6 V. Linear sweep voltammetry (LSV) was conducted at both 20 °C and 45 °C with a 12 mm carbon-coated Al foil disc (22 µm, SDX, ShowaDenko) as working electrode, and a 15 mm Li disk as counter electrode and the same separator electrolyte setup as described above. The surface area of the working electrode was calculated based on the electrode diameter. The voltage scan rate was 0.1 mV s<sup>-1</sup>, scanning from the OCV to 5 V vs. Li/Li<sup>+</sup>. The LNMO charge and discharge voltage profiles were obtained by cycling a LNMO||LP40||Li cell in a 3.5–5 V range on an Arbin BT cycler at room temperature at C/10 rate. The synthetic charge-discharge profile voltammetry (SCPV) measurements were carried out according to a procedure described previously.<sup>[47]</sup> In short, the SCPV method operates by cycling the electrolytes against inert electrodes using the imported cycling curve of the battery cell. These measurements were performed in a two-electrode cell format using 13 mm ø carbon coated aluminum foil as working electrode and a 15 mm ø Li foil as counter and reference electrode. When using LP40 electrolyte, a Celgard 2500 separator was utilized in a coin cell format, while in the case of the ILE, a glass fiber separator was employed in a pouch cell format. The rate testing of LNMO||graphite full cells was conducted both at 20 °C and at 45 °C (the latter representing an accelerated ageing scenario) by galvanostatic charge discharge cycling on a Biologic BCS 805 between 3.5 and 4.8 V vs. Li/Li<sup>+</sup> using C-rates C/10, C/5, C/2, 1 C, and 2 C. The charging rate was limited to maximum C/2. The long-term galvanostatic cycling was performed with the same voltage cut-offs as for the rate testing, and with a C-rate of C/2 after the formation cycles that were conducted with a C-rate of C/10. Additionally, two diagnostic cycles of C/10 were included every 25 cycles to obtain information relating to the origin of capacity decay: Kinetic limitations will be revealed by the regaining of capacity at lower C-rates, while capacity decay due to loss of Li inventory will be less affected by the current density.

The LNMO cells cycled up to 40 cycles using LP40 and ILE at room temperature were both disassembled and the LNMO electrodes were washed with dimethyl carbonate (DMC) to eliminate any electrolyte residues and thereafter dried. The X-ray photoelectron spectroscopy (XPS) sample preparation, including the LNMO pristine electrode, was performed inside a glove box to avoid air contact. The XPS sample holder was vacuum sealed and then transferred to the measurement chamber. The measurements were carried out in a Kratos Axis Supra + X-ray photoelectron spectrometer with an Al K $\alpha$  (1486.6 eV) X-ray source. The data analysis was performed using CasaXPS software with the hydrocarbon peak energy corrected to 284.8 eV and the complete spectra were

calibrated versus the hydrocarbon peak. Data are presented as measured without any intensity normalization.

For post-mortem Scanning electron microscopy (SEM) and Energy dispersive X-ray spectroscopy (EDS) characterization, LNMO||graphite cells were disassembled after approximately 1200 cycles at 45 °C, and the electrodes removed and washed with propylene carbonate (PC) to remove residues. Samples were mounted for analysis and transferred to the instrument location under inert conditions, with a brief exposure (approx. 30 secs) to air whilst loading into the electron microscope. Data were collected using a FEI Apreo FEG-SEM equipped with an Oxford Aztec EDS system. X-ray maps were generated using the K-edge X-ray data for all elements except Cu, for which the L-edge was used in order to reduce sampling depth and increase spatial resolution. The Oxford-Instruments proprietary "TruMap" algorithm was used to deconvolute peak overlaps and subtract background counts.

## Acknowledgements

This work was performed within MoZEEs, a Norwegian Centre for Environment Friendly Energy Research (FME), co-sponsored by the Research Council of Norway (project no. 257653) and 40 partners from research, industry, and public sector. A. M. and D. B. acknowledge support from the STandUP for Energy consortium and Batteries Sweden. J. R. T. and N. P. W. acknowledge the research council of Norway for funding of the strategic institute project Enerlyte through the basic grant received by SINTEF Industry.

## Conflict of Interests

The authors declare no conflict of interest.

## Data Availability Statement

The data that support the findings of this study are available from the corresponding author upon reasonable request.

**Keywords:** energy conversion • high-voltage cathode • ionic liquid • lithium-ion battery • sustainable chemistry

- [1] W. Li, Y. G. Cho, W. Yao, Y. Li, A. Cronk, R. Shimizu, M. A. Schroeder, Y. Fu, F. Zou, V. Battaglia, A. Manthiram, M. Zhang, Y. S. Meng, *J. Power Sources* **2020**, *473*, 228579.
- [2] J. Song, D. W. Shin, Y. Lu, C. D. Amos, A. Manthiram, J. B. Goodenough, *Chem. Mater.* **2012**, *24*, 3101–3109.
- [3] M. Wentker, M. Greenwood, J. Leker, *Energies* **2019**, *12*, 504.
- [4] T. F. Yi, J. Mei, Y. R. Zhu, *J. Power Sources* **2016**, *316*, 85–105.
- [5] N. P. W. Pieczonka, Z. Liu, P. Lu, K. L. Olson, J. Moote, B. R. Powell, J.-H. Kim, *J. Phys. Chem. C* **2013**, *117*, 15947–15957.
- [6] X. L. Xu, S. X. Deng, H. Wang, J. B. Liu, H. Yan, *Nano-Micro Lett.* **2017**, *9*, 1–19.
- [7] G. Liang, V. K. Peterson, K. W. See, Z. Guo, W. K. Pang, *J. Mater. Chem. A* **2020**, *8*, 15373–15398.
- [8] K. Xu, *Chem. Rev.* **2014**, *114*, 11503–11618.
- [9] J. B. Goodenough, Y. Kim, *J. Power Sources* **2011**, *196*, 6688–6694.
- [10] X. Fan, C. Wang, *Chem. Soc. Rev.* **2021**, *50*, 10486–10566.

- [11] U. Heider, R. Oesten, M. Jungnitz, *J. Power Sources* **1999**, *81–82*, 119–122.
- [12] K. Kanayama, S. Takahashi, S. Morikura, H. Nakamura, T. Tezuka, K. Maruta, *Combust. Flame* **2022**, *237*, 111810.
- [13] K. Xu, *Chem. Rev.* **2004**, *104*, 4303–4417.
- [14] A. Abouimrane, J. Ding, I. J. Davidson, *J. Power Sources* **2009**, *189*, 693–696.
- [15] S. T. Myung, Y. Hitoshi, Y. K. Sun, *J. Mater. Chem.* **2011**, *21*, 9891–9911.
- [16] P. Meister, X. Qi, R. Kloepsch, E. Krämer, B. Streipert, M. Winter, T. Placke, *ChemSusChem* **2017**, *10*, 804–814.
- [17] X. Zhang, T. M. Devine, *J. Electrochem. Soc.* **2006**, *153*, B344.
- [18] A. Hofmann, A. Höweling, N. Bohn, M. Müller, J. R. Binder, T. Hanemann, *ChemElectroChem* **2019**, *6*, 5255–5263.
- [19] H. Zhi, L. Xing, X. Zheng, K. Xu, W. Li, *J. Phys. Chem. Lett.* **2017**, *8*, 6048–6052.
- [20] J. Wang, Y. Yamada, K. Sodeyama, C. H. Chiang, Y. Tateyama, A. Yamada, *Nat. Commun.* **2016**, *7*, 1–9.
- [21] Y. Yamada, J. Wang, S. Ko, E. Watanabe, A. Yamada, *Nat. Energy* **2019**, *4*, 269–280.
- [22] K. K. Fu, Y. Gong, B. Liu, Y. Zhu, S. Xu, Y. Yao, W. Luo, C. Wang, S. D. Lacey, J. Dai, Y. Chen, Y. Mo, E. Wachsman, L. Hu, *Sci. Adv.* **2017**, *3*, 1–12.
- [23] W. Liu, N. Liu, J. Sun, P. C. Hsu, Y. Li, H. W. Lee, Y. Cui, *Nano Lett.* **2015**, *15*, 2740–2745.
- [24] Y. Zhao, C. Wu, G. Peng, X. Chen, X. Yao, Y. Bai, F. Wu, S. Chen, X. Xu, *J. Power Sources* **2016**, *301*, 47–53.
- [25] A. Ahniyaz, I. de Meatza, A. Kvasha, O. Garcia-Calvo, I. Ahmed, M. F. Sgroi, M. Giuliano, M. Dotoli, M.-A. Dumitrescu, M. Jahn, N. Zhang, *Adv. Appl. Energy* **2021**, *4*, 100070.
- [26] J. Zhao, J. Zhang, P. Hu, J. Ma, X. Wang, L. Yue, G. Xu, B. Qin, Z. Liu, X. Zhou, G. Cui, *Electrochim. Acta* **2016**, *188*, 23–30.
- [27] Y. Ma, J. Ma, J. Chai, Z. Liu, G. Ding, G. Xu, H. Liu, B. Chen, X. Zhou, G. Cui, L. Chen, *ACS Appl. Mater. Interfaces* **2017**, *9*, 41462–41472.
- [28] J. Chen, J. Wu, X. Wang, A. Zhou, Z. Yang, *Energy Storage Mater.* **2021**, *35*, 70–87.
- [29] M. Galinski, A. Lewandowski, I. Stepniak, *Electrochim. Acta* **2006**, *51*, 5567–5580.
- [30] N. Chawla, N. Bharti, S. Singh, *Batteries* **2019**, *5*, 1–25.
- [31] D. M. Fox, J. W. Gilman, A. B. Morgan, J. R. Shields, P. H. Maupin, R. E. Lyon, H. C. De Long, P. C. Trulove, *Ind. Eng. Chem. Res.* **2008**, *47*, 6327–6332.
- [32] R. S. Künnel, A. Balducci, *J. Power Sources* **2014**, *249*, 163–171.
- [33] Y. Yamada, C. H. Chiang, K. Sodeyama, J. Wang, Y. Tateyama, A. Yamada, *ChemElectroChem* **2015**, *2*, 1687–1694.
- [34] M. Moreno, E. Simonetti, G. B. Appetecchi, M. Carewska, M. Montanino, G.-T. Kim, N. Loeffler, S. Passerini, *J. Electrochem. Soc.* **2017**, *164*, A6026–A6031.
- [35] A. I. Bhatt, A. S. Best, J. Huang, A. F. Hollenkamp, *J. Electrochem. Soc.* **2010**, *157*, A66.
- [36] G. B. Appetecchi, M. Montanino, A. Balducci, S. F. Lux, M. Winter, S. Passerini, *J. Power Sources* **2009**, *192*, 599–605.
- [37] H. Matsumoto, H. Sakaebi, K. Tatsumi, M. Kikuta, E. Ishiko, M. Kono, *J. Power Sources* **2006**, *160*, 1308–1313.
- [38] C. J. Wu, P. C. Rath, J. Patra, D. Bresser, S. Passerini, B. Umesh, Q. F. Dong, T. C. Lee, J. K. Chang, *ACS Appl. Mater. Interfaces* **2019**, *11*, 42049–42056.
- [39] P. C. Rath, Y. W. Wang, J. Patra, B. Umesh, T. J. Yeh, S. Okada, J. Li, J. K. Chang, *Chem. Eng. J.* **2021**, *415*, DOI 10.1016/j.cej.2021.128904.
- [40] H. J. Lee, Z. Brown, Y. Zhao, J. Fawdon, W. Song, J. H. Lee, J. Ihli, M. Pasta, *Chem. Mater.* **2021**, *33*, 1238–1248.
- [41] D. T. Rogstad, M.-A. Einarsrud, A. M. Svensson, *J. Electrochem. Soc.* **2021**, *168*, 110506.
- [42] D. M. Piper, T. Evans, K. Leung, T. Watkins, J. Olson, S. C. Kim, S. S. Han, V. Bhat, K. H. Oh, D. A. Buttry, S. H. Lee, *Nat. Commun.* **2015**, *6*, 1–10.
- [43] E. Luais, F. Ghamouss, J. Sakai, T. Defforge, G. Gautier, F. Tran-Van, *J. Solid State Electrochem.* **2019**, *23*, 937–941.
- [44] J. Guo, D. Dong, J. Wang, D. Liu, X. Yu, Y. Zheng, Z. Wen, W. Lei, Y. Deng, J. Wang, G. Hong, H. Shao, *Adv. Funct. Mater.* **2021**, *31*, 1–65.
- [45] S. Seki, Y. Kobayashi, H. Miyashiro, Y. Ohno, Y. Mita, N. Terada, P. Charest, A. Guerfi, K. Zaghib, *J. Phys. Chem. C* **2008**, *112*, 16708–16713.
- [46] H. Matsumoto, H. Sakaebi, K. Tatsumi, M. Kikuta, E. Ishiko, M. Kono, *J. Power Sources* **2006**, *160*, 1308–1313.
- [47] A. Mathew, M. J. Lacey, D. Brandell, *J. Power Sources* **2021**, *11*, 100071.
- [48] D. S. Lu, L. B. Yuan, J. L. Li, R. Q. Huang, J. H. Guo, Y. P. Cai, *J. Electroanal. Chem.* **2015**, *758*, 33–38.
- [49] J. Kasnatscheew, B. Streipert, S. Röser, R. Wagner, I. Cekic Laskovic, M. Winter, *Phys. Chem. Chem. Phys.* **2017**, *19*, 16078–16086.
- [50] D. T. Rogstad, M.-A. Einarsrud, A. M. Svensson, *J. Electrochem. Soc.* **2022**, *169*, 110531.
- [51] S. H. Ng, C. Vix-Guterl, P. Bernardo, N. Tran, J. Ufheil, H. Buqa, J. Dentzer, R. Gadiou, M. E. Spahr, D. Goers, P. Novák, *Carbon* **2009**, *47*, 705–712.
- [52] S. Solchenbach, M. Wetjen, D. Pritzl, K. U. Schwenke, H. A. Gasteiger, *J. Electrochem. Soc.* **2018**, *165*, A512–A524.
- [53] S. J. Kang, K. Park, S. H. Park, H. Lee, *Electrochim. Acta* **2018**, *259*, 949–954.
- [54] G. G. Eshetu, T. Diemant, S. Grugeon, R. J. Behm, S. Laruelle, M. Armand, S. Passerini, *ACS Appl. Mater. Interfaces* **2016**, *8*, 16087–16100.
- [55] S. Klein, P. Harte, S. van Wickeren, K. Borzutzki, S. Röser, P. Bärmann, S. Nowak, M. Winter, T. Placke, J. Kasnatscheew, *Cell Rep. Phys. Sci.* **2021**, *2*, DOI 10.1016/j.xcrp.2021.100521.
- [56] J. C. Burns, A. Kassam, N. N. Sinha, L. E. Downie, L. Solnickova, B. M. Way, J. R. Dahn, *J. Electrochem. Soc.* **2013**, *160*, A1451–A1456.
- [57] B. Aktekin, R. Younesi, W. Zipprich, C. Tengstedt, D. Brandell, K. Edström, *J. Electrochem. Soc.* **2017**, *164*, A942–A948.
- [58] R. Tatara, P. Karayalali, Y. Yu, Y. Zhang, L. Giordano, F. Maglia, R. Jung, J. P. Schmidt, I. Lund, Y. Shao-Horn, *J. Electrochem. Soc.* **2019**, *166*, A5090–A5098.
- [59] W. Liu, J. Li, W. Li, H. Xu, C. Zhang, X. Qiu, *Nat. Commun.* **2020**, *11*, 3629.
- [60] B. Aktekin, M. J. Lacey, T. Nordh, R. Younesi, C. Tengstedt, W. Zipprich, D. Brandell, K. Edstrom, *J. Phys. Chem. C* **2018**, *122*, 11234–11248.
- [61] H. Li, T. Yamaguchi, S. Matsumoto, H. Hoshikawa, T. Kumagai, N. L. Okamoto, T. Ichitsubo, *Nat. Commun.* **2020**, *11*, 1584.

Manuscript received: March 3, 2023

Revised manuscript received: May 4, 2023

Accepted manuscript online: May 5, 2023

Version of record online: June 1, 2023